Detection of neuritic plaques in Alzheimer's disease by magnetic resonance microscopy

Helene Benveniste[†‡§¶], Gillian Einstein[§], Katie R. Kim[†], Christine Hulette[§‖], and G. Allan Johnson[†]

Departments of [†]Radiology, [‡]Anesthesiology, [§]Neurobiology, and [‖]Medicine, Duke University Medical Center, Durham, NC 27710

Edited by Dale Purves, Duke University Medical Center, Durham, NC, and approved September 24, 1999 (received for review July 8, 1999)

Magnetic resonance microscopy (MRM) theoretically provides the spatial resolution and signal-to-noise ratio needed to resolve neuritic plaques, the neuropathological hallmark of Alzheimer's disease (AD). Two previously unexplored MR contrast parameters, T2* and diffusion, are tested for plaque-specific contrast to noise. Autopsy specimens from nondemented controls (n = 3) and patients with AD (n = 5) were used. Three-dimensional T2* and diffusion MR images with voxel sizes ranging from 3×10^{-3} mm^3 to 5.9×10^{-5} mm^3 were acquired. After imaging, specimens were cut and stained with a microwave king silver stain to demonstrate neuritic plaques. From controls, the alveus, fimbria, pyramidal cell layer, hippocampal sulcus, and granule cell layer were detected by either T2* or diffusion contrast. These structures were used as landmarks when correlating MRMs with histological sections. At a voxel resolution of 5.9×10^{-5} mm^3, neuritic plaques could be detected by T2*. The neuritic plaques emerged as black, spherical elements on T2* MRMs and could be distinguished from vessels only in cross-section when presented in three dimension. Here we provide MR images of neuritic plaques *in vitro*. The MRM results reported provide a new direction for applying this technology *in vivo*. Clearly, the ability to detect and follow the early progression of amyloid-positive brain lesions will greatly aid and simplify the many possibilities to intervene pharmacologically in AD.

Neuritic plaques, which are the neuropathological hallmark of Alzheimer's disease (AD), have not yet been visualized in the brain by MRI. Lack of detection by MRI is due to neuritic plaques' small size (5–200 μm) and unknown magnetic resonance (MR) parameters. To resolve neuritic plaques, the spatial resolution (voxel size) of the images must be at least 0.2^3 mm^3 = 8×10^{-3} mm^3. Stronger than normal magnetic field gradients (>200 T/m) would be required to achieve such small voxels.** For comparison, conventional large-bore clinical system gradients are capable of only 10–50 mT/m. In addition to strong gradients, a high magnetic field (4–10 T) would be necessary to partially compensate for loss of signal-to-noise ratio (SNR) in small voxels.

Magnetic resonance microscopy (MRM) theoretically provides the spatial resolution and SNR needed to visualize neuritic plaques. MRM is founded on the same fundamental principle as MRI but produces images with higher than normal spatial resolution because of the use of strong magnetic field gradients (200–800 mT/m) and specialized radio frequency (RF) coils (1, 2). For example, a spatial resolution of 20 μm^3 per voxel has been achieved in formalin-fixed embryos (1, 3).

Assuming that adequate spatial resolution and SNR is attainable with MRM, neuritic plaque visualization still may be constrained by an insufficient contrast-to-noise ratio (CNR). By definition, CNR depends on the different signal between two structures of interest, for example, neuritic plaques and the surrounding brain matrix. A typical neuritic plaque consists of a central core of extracellular amyloid fibrils intermingled with and surrounded by abnormal neuronal processes (4, 5). Some neuritic plaques are known to contain metal particles, such as iron (6, 7).

It is difficult to predict which MR parameter would produce a plaque-specific signal. A previous MRM study using T1- and T2-weighted contrast did not reveal plaques in formalin-fixed hippocampi from patients with known AD (8). The extracellular location of amyloid fibrils in white matter areas suggests that diffusion contrast might visualize these particles. Alternatively, T2* contrast might reveal plaques if they induce local magnetic field inhomogeneities, particularly in those plaques containing iron.

In our study, we addressed the question of how best to resolve neuritic plaques *in vitro* with MRM if both spatial resolution and SNR are optimized. We tested two previously unexplored MRM contrast parameters, T2* and diffusion, for plaque-specific CNR. All experiments were conducted on formalin-fixed human specimens from nondemented control subjects and subjects with known AD by using a 7.1-T magnet, strong magnetic field gradients, and a 1-cm Helmholz RF imaging coil.

Materials and Methods

Cases. Hippocampal specimens from three nondemented controls and five patients with a neuropathological diagnosis of AD were randomly selected from cases received between 1993 and 1996 at the Kathleen Price Bryan Brain Bank at the Bryan Alzheimer's Disease Research Center at Duke University and the University of Miami Brain Bank (compare Table 1). Brains were processed routinely through the Rapid Autopsy Program (9), examined, and evaluated according to Consortium to Establish a Registry for Alzheimer's Disease criteria (10). Neurofibrillary change was staged according to Braak and Braak (11).

MR Microscopy. For imaging, the tissue specimens from each of the eight subjects were trimmed to fit into a 1-cm-diameter acrylic well designed to center specimens within the RF coil (see below). The well was filled with Fomblin (perfluoropolyether; Ausimont, Morristown, NJ) and covered with a glass coverslip by using extreme care to avoid air bubbles entering the well. Fomblin was used as an embedding medium to limit tissue dehydration as well as susceptibility effects at the surface of the specimen. Imaging was performed on a 7.1-T (300 MHz), 12-cm bore, Oxford superconducting magnet. The magnet is equipped with actively shielded gradients capable of 850 mT/m. The RF coil consisted of two copper loops positioned to constitute a Helmholtz pair (12). The B1 field between the two loops is known to be very homogeneous and, therefore, well suited for imaging at high magnetic field (12). All scans were performed at a magnet bore temperature of 21.1°C (controlled by an automated water cooler).

Because optimal spatial resolution for detection of neuritic plaques was unknown, we started by acquiring three-dimensional

This paper was submitted directly (Track II) to the PNAS office.

Abbreviations: SNR, signal-to-noise ratio; AD, Alzheimer's disease; MRM, magnetic resonance microscopy; CNR, contrast-to-noise ratio; RF, radio frequency; 3D, three-dimensional; MK, microwave king; GRASS, gradient-recalled acquisition steady state.

[¶]To whom reprint requests should be addressed at: Department of Anesthesiology, Box 3094, Duke University Medical Center, Durham, NC 27710. E-mail: hb@orion.mc.duke.edu.

**As an example, the size of a pixel along the frequency encoding axis, Δx, is given by the equation $\Delta x = 1/T_{ac} \cdot 2\pi/\gamma G_r$. G_r is the amplitude of the frequency-encoding gradient, T_{ac} is the acquisition time, and γ is the proton gyromagnetic ratio, 2.6752×10^8 T^{-1} s^{-1}. Thus, for 50-μm-wide plaques (Δx) and $T_{ac} \approx 2$ ms, G_r would need to be at least $[1/0.002s \cdot 2\pi/(2.6752 \times 10^8\ T^{-1}\ s^{-1} \cdot 0.005\ cm)] \times 10{,}000$ gauss/T $\approx$ 230 mT/m.

The publication costs of this article were defrayed in part by page charge payment. This article must therefore be hereby marked "*advertisement*" in accordance with 18 U.S.C. §1734 solely to indicate this fact.

Table 1. Hippocampal specimens

Case no.	Braak and Braak stage	Clinical diagnosis and age
739 BB# 96-25	I	Control: 93 yr
676 BB# 95-39	I	Control: 60 yr
516 BB# 93-39	II	Control: 85 yr
667 A# 95-215	III	Demented: 95 yr
764 A# 96-171	IV	Demented: 83 yr
658 BB# 95-27	V	Demented: 82 yr
511 A# 93-175	VI	Demented: 72 yr
659 BB# 95-28	VI	Demented: 74 yr

(3D) proton stains with voxel sizes that theoretically would be sufficiently large to detect plaques >80 μm across. However, if plaques were not visualized on these proton stains, the next AD specimen would be scanned at still higher resolution. Two different MR contrast parameters were explored: T2* and diffusion. One hippocampal control specimen was used in a preliminary series of imaging experiments designed to determine suitable MR parameters for the study. For T2* images, a gradient-recalled acquisition steady-state (GRASS) 3D sequence was used with an echo time (TE) of 8–9 ms and a repetition time (TR) of 150 ms TR. The pulse flip angle was varied in the first acquisition series, and for a given voxel size, a pulse flip angle of 25° yielded higher SNR compared with 35° and 45°. However, a pulse flip angle of 35° was chosen for all subsequent scans because of superior CNR.

For diffusion images, a Stejskal and Tanner (13) diffusion-weighted 3D spin-echo pulse sequence was used (20-ms TE, 800- to 1,000-ms TR, and diffusion gradients of 350 mT/m applied in the slice direction), yielding a b value of 965 mm^2/s. In the preliminary data acquisitions, the diffusion gradients were also applied in the frequency-encoding axis. With the diffusion gradient applied in this direction, the alveus appeared brighter. However, no additional hippocampal anatomy was revealed by this maneuver. In all subsequent scans, the diffusion gradients were applied in the slice direction. To check the accuracy and reliability of the diffusion measurements, the diffusion coefficient of a water phantom was obtained previously by using the same sequence; the diffusion coefficient of water at 21°C amounted to $2.3 \pm 0.1 \times 10^{-3}$ mm^2/s, which is in agreement with values reported in the literature.

All raw data were reconstructed by Fourier transform and displayed as magnitude images. In the following, we refer to T2* and diffusion-weighted MR images as either T2* or diffusion "proton stains" (1). The SNR in all images were calculated by the method described by Edelstein *et al.* (14) by using a signal region of 4×4 pixels and a noise region of 50×50 pixels to ensure an accuracy within 10%. The SNR was calculated across the entire image and the maximum SNR for each image was extracted. All SNR measurements were performed by the same investigator (K.R.K.).

Histology. After imaging, specimens were dehydrated and embedded in paraffin. The entire paraffin-embedded specimen was cut serially in 10-μm-thick sections on a sliding microtome. Every tenth section was stained with a microwave king (MK) silver stain used for neuropathologic diagnosis of AD and demonstration of neuritic plaques (15).

Image Processing. All histological sections were digitized at a resolution of 10 μm/pixel (2,700 dpi) by using a Polaroid SprintScan 35-mm scanner (Polaroid) and a PathScan Enabler System (Meyer Instruments, Houston, TX) attached to a Power/Tower Pro 225 Macintosh-compatible computer (PowerComputing, Round Rock, TX). All digitized images were calibrated by means of a micrometer scanned at the same Polaroid SprintScan 35-mm apparatus. For higher-resolution images of histological sections, we used a Color Digital Camera (SPOT; Diagnostic Instruments, Sterling Heights, MI) attached to an Olympus BX50 system microscope (Olympus, New Hyde Park, NY). Three-dimensional images were volume-rendered and reformatted by using VoxelView ULTRA 2.5 software (Vital Images, Fairfield, IA) on a Reality Engine2 Workstation (Silicon Graphics, Mountain View, CA). Volume-rendered and/or color-coded images from a variety of orientations and reformatted slices from varying planes were captured on the Silicon Graphics workstation and moved to the Macintosh computer for annotating by using Adobe PHOTOSHOP 4.0 4.0.1 PowerPC (Adobe Systems, Mountain View, CA).

Matching of Histological Sections with MRM Images. All histological sections expanded slightly during the histological processing, and it was not possible to match the histological sections with the MRM images by using superimposition. Thus, the process of matching digitized histological sections with MR images was based on pattern recognition and consisted of several steps. First, several MRM images and digitized histological sections close to the center of the specimen were displayed side by side by using PHOTOSHOP and scrutinized for matching structures. For example, in both normal and AD hippocampal specimens, the shape of vessels, hippocampal sulcus, and the granule cell layer of the dentate gyrus were helpful structures to use for matching. In addition, in AD specimens, the arrangement of plaques within the tissue (e.g., plaques in a row or in a cluster) were used as landmarks. Once convincing corresponding landmarks were found, the approximation between histological sections and MRM images was improved further by modifying the imaging plane in the volumetric MR data. Frequently, modification of the imaging plane was required because the cutting plane of the histological sections deviated slightly from the imaging plane. The imaging plane was manipulated by means of VoxelView ULTRA 2.5 software (this process was only done on 3D data sets with isotropic voxels). The 3D display was also useful to identify vessels within the specimen and to differentiate between vessels and spherical, plaque-like structures. The matching process was performed independently by two of the investigators (H.B. and K.R.K.).

Results

Three of the 3D scans could not be used in the final data analysis because of air-induced artifacts in the images. Another five 3D scans were too "noisy" to be meaningful for data analysis (this was most often associated with a low SNR).

Nondemented Controls. The appearance of hippocampal anatomy on T2* proton stains was different from that of diffusion proton stains. First, on diffusion proton stains, the granule cell layer of the dentate gyrus and pyramidal cell layers were visible as distinct, low-signal intensity bands. In contrast, on T2* proton stains, the granule cell layer was either invisible or appeared as a faint, bright line. Further, myelin-rich areas such as the fimbria and alveus generally were more apparent on T2* proton stains.

A typical T2* proton stain and corresponding MK silver-stained hippocampal section from a control subject are shown in Fig. 1. On the T2* proton stain, the hippocampal sulcus emerges as a dark, low-signal-intensity band. Other band-like structures are apparent above and below the hippocampal sulcus (compare Fig. 1). These probably represent myelin-rich pathways; for example, the pathway between the entorhinal area and the CA1 region is known to pass through the molecular layer of the gyrus dentatus (16). The solid, black band between the CA3 and the CA4 region on the T2* proton stain (asterisk, Fig. 1) probably represents part of the polysynaptic intrahippocampal pathway (e.g., Schaffer collaterals). Most vessels apparent on the MK stain are not visible on the corresponding T2* proton stain. Vessels in cross-section appear as black, solid structures on T2* proton stains. On this particular T2* proton stain, the granule cell layer cannot be identified (compare Fig. 1).

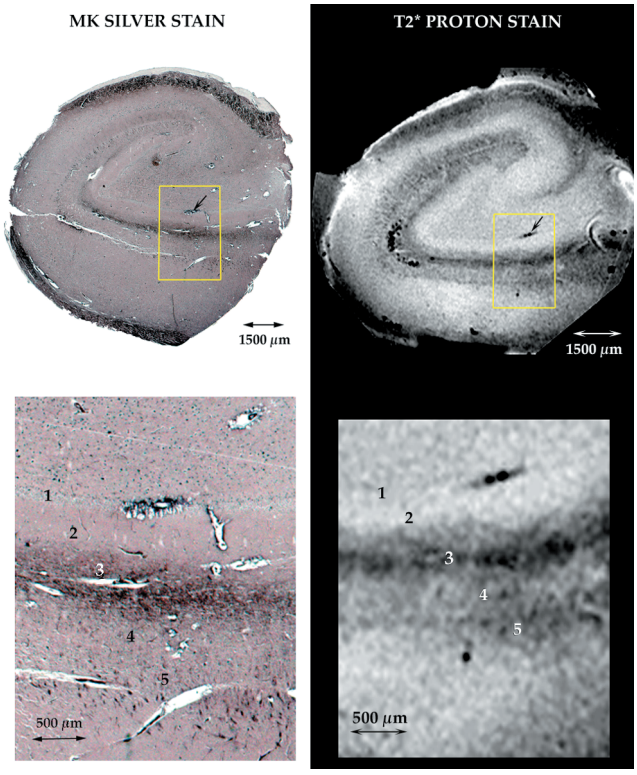

Fig. 1. (*Upper*) A representative coronal hippocampal MK silver-stained section and corresponding T2* proton stain from nondemented control subject. The resolution of the T2* proton stain was 1.2×10^{-4} mm^3, and the average SNR was 54:1. (*Lower*) Hippocampal subfields, indicated by numbers, are based on their known anatomical location: 1, granule cell layer of gyrus dentatus; 2, molecular layer of gyrus dentatus; 3, vestigial hippocampal sulcus; 4, molecular layer of the CA1; 5, stratum lacunosum of the CA1. Note that multiple vessels present on the MK-stained section do not consistently emerge on the T2* proton stain.

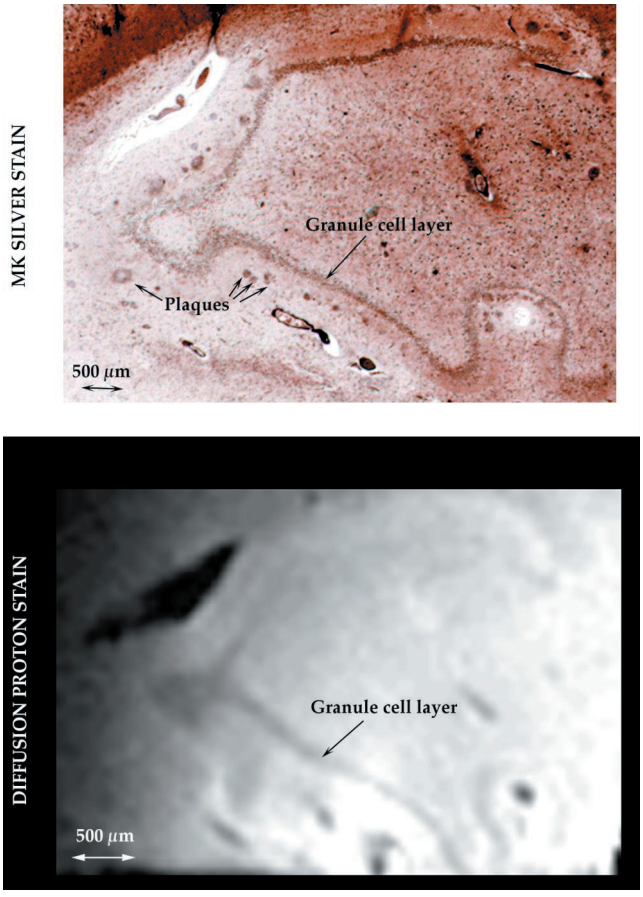

Fig. 2. Corresponding 10-μm-thick MK silver-stained hippocampal section and 80-μm-thick diffusion proton stain from an AD subject (Braak and Braak stage III; ref. 11). The voxel size in the diffusion proton stain is 4.7×10^{-4} mm^3, and the average SNR is 69. The granule cell layer is recognized as a black, discrete band. On the MK silver-stained section, plaques of the diffuse type without prominent amyloid cores (shorter arrows) can be seen in their typical location, that is, in the molecular layer of the dentate gyrus, approximately two-thirds of the way from the top of the hippocampal sulcus. Plaque-like structures cannot be recognized on the corresponding diffusion proton stain.

AD Cases: Diffusion Proton Stains. Diffusion proton stains were performed on four AD specimens at progressively smaller voxel size: 3×10^{-3} mm^3, 4.7×10^{-4} mm^3, 1.2×10^{-4} mm^3, and 5.9×10^{-5} mm^3 (compare Table 2). At 3×10^{-3} mm^3, only major anatomical landmarks such as the alveus and hippocampal sulcus were recognized and no plaque-like structures could be identified (results not shown). Fig. 2 shows a diffusion proton stain acquired at a voxel resolution of 4.7×10^{-4} mm^3 and a corresponding MK silver-stained section from an AD specimen. As in tissue obtained from nondemented controls, the granule cell layer emerges as a solid, black band on the diffusion proton stain. Further, larger vessels emerge as dense, black structures, often with a halo. On the MK silver stain, large, 70- to 170-μm-wide plaques of the diffuse type can be seen in the molecular layer of the dentate gyrus, two-thirds down from the hippocampal sulcus (17). In a corresponding location on the diffusion proton stain, plaque-like structures cannot be recognized (compare Fig. 2). On other adjacent, MK-stained sections, neuritic plaques were seen within the CA4 region. Again, these could not be located on corresponding proton stains.

As expected, the average SNR of the diffusion proton stains decreased with an increase in spatial resolution. For example, at a voxel size of 1.2×10^{-4} mm^3, the SNR amounted to 34:1, compared with 69:1 with voxel of 4.7×10^{-4} mm^3 (same scan time, compare Table 2). On diffusion proton stains acquired at a voxel size of 1.2×10^{-4} mm^3, an adequate number of anatomical landmarks were available for successful matching to the histological sections. However, similar to diffusion proton stains with a spatial resolution of 4.7×10^{-4} mm^3, no plaque-like structures could be identified. At the highest spatial resolution, that is, 5.9×10^{-5} mm^3, the diffusion images generally were too noisy (SNR <20:1) for meaningful data analysis.

Table 2. Diffusion proton stains acquired from AD specimens

Specimen no.	Pulse sequence	Voxel size, mm^3	Acquisition time, hr	SNR
511	Diffusion	3×10^{-3}	14.6	63:1
667	Diffusion	4.7×10^{-4}	14.6	69:1
511	Diffusion	4.7×10^{-4}	7.3	36:1
658	Diffusion	1.2×10^{-4}	4.6	34:1
764	Diffusion	5.9×10^{-5}	18.2	18:1
764	Diffusion	5.9×10^{-5}	18.2	14:1

Alzheimer's Cases: T2* Proton Stains. T2* protons stains were performed on four of the five AD specimens. At spatial resolutions of 3×10^{-3} mm^3 and 1.2×10^{-4} mm^3, no individual plaque-like structures could be detected on T2* proton stains. For example, Fig. 3 shows T2* proton stains acquired at progressively higher spatial resolution from an AD specimen. A row of neuritic plaques can be seen in front of a large, crescent-shaped vessel on the MK silver-stained section. In a corresponding location on the T2* proton stain

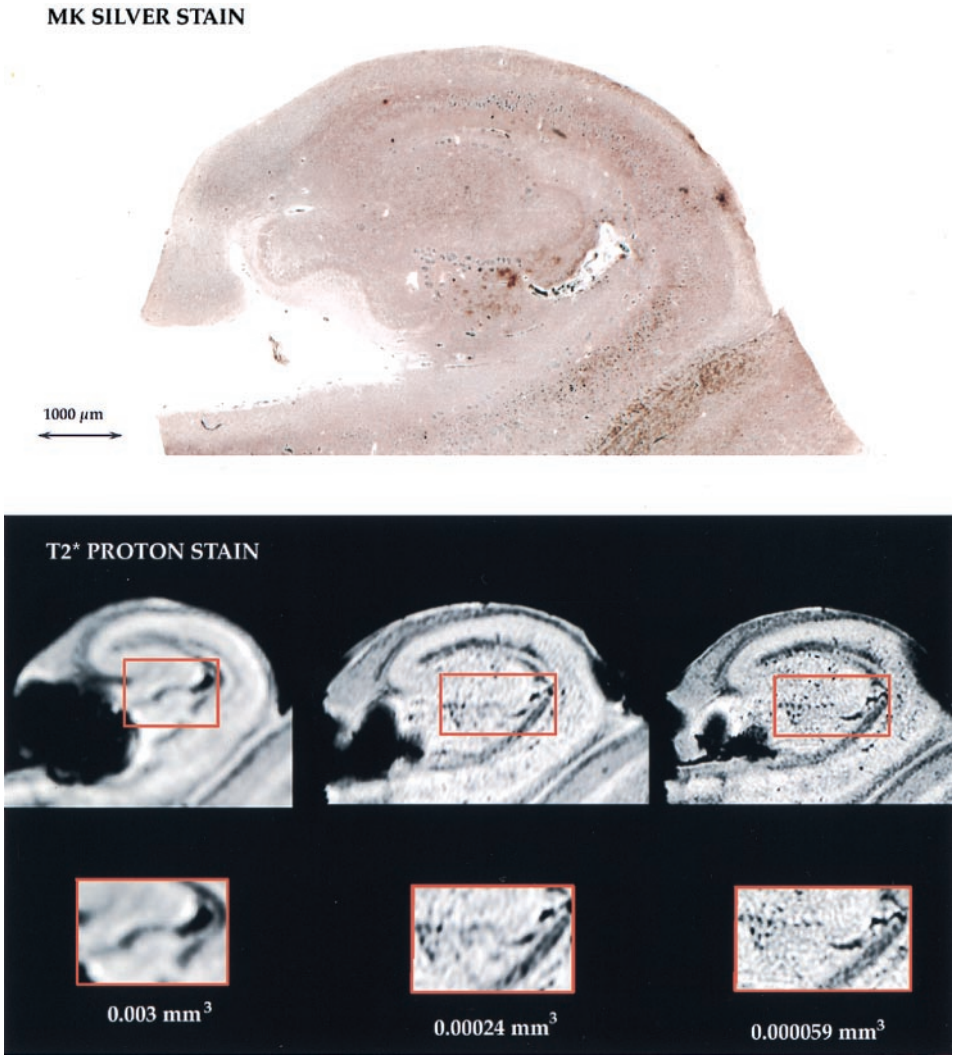

Fig. 3. (*Upper*) T2* proton-stained, MK-stained hippocampal section from an AD subject. Neuritic plaques with prominent amyloid cores can be seen in multiple locations. For example, in front of a crescent-shaped vessel, a row of plaque can be seen. (*Lower*) Corresponding T2* proton stains acquired of this specimens at progressively higher spatial resolution; at voxel sizes of 3×10^{-3} mm^3 and 2.4 mm^3, the row of plaques cannot be seen in front of the large vessel. However, at a voxel size of 5.9×10^{-5} mm^3, individual plaque-like structures can be easily identified. The plaques on the MK silver-stained section measure from 50 to 150 μm across. On the T2* proton stain, plaque-like structures measure from 100 to 150 μm across.

acquired at the lowest spatial resolution, 3×10^{-3} mm^3, the crescent-shaped vessel can barely be appreciated and individual plaque-like structures are not seen. At 2.4×10^{-3} mm^3, the shape of the vessel is better characterized. However, at 5.9×10^{-5} mm^3, well defined individual, plaque-like structures can be can identified in front of the crescent-shaped vessel. The diameter of the neuritic plaques on the MK stain vary from 50–150 μm across; on the T2* stain, the plaque-like structures measure approximately 100 μm across.

Fig. 4 shows MK silver-stained and corresponding T2* proton-stained sections from another AD hippocampal specimen. The granule cell layer is visible as a faint, bright band on this particular T2* proton stain (compare Fig. 4). On the MK silver-stained section, a row of neuritic plaques can be seen in parallel to the granule cell layer. In a corresponding location on the T2* proton stain acquired at a voxel resolution of 5.9×10^{-5} mm^3, a row of black, rounded elements can be located above the brighter band representing the granule cell layer.

A sufficient SNR was essential for visualization of plaque-like structures on T2* proton stains. For example, in T2* proton stains from one of the AD specimens acquired at 5.9×10^{-5} mm^3, no plaques could be detected because the SNR was too low for meaningful data analysis (compare Table 3).

Discussion

In this study we show that neuritic plaques in hippocampal tissue from subjects with AD can be detected noninvasively by using

Table 3. T2* proton stains acquired from AD specimens

Specimen no.	Pulse sequence	Voxel size, mm^3	Acquisition time, hr	SNR
511	GRASS	3×10^{-3}	2.7	128:1
511	GRASS	2.4×10^{-4}	5.6	96:1
658	GRASS	1.2×10^{-4}	5.5	42:1
764	GRASS	5.9×10^{-5}	5.5	20:1
764	GRASS	5.9×10^{-5}	10.9	28:1
764	GRASS	5.9×10^{-5}	10.9	27:1
511	GRASS	5.9×10^{-5}	10.9	38:1
659	GRASS	5.9×10^{-5}	10.9	24:1
659	GRASS	5.9×10^{-5}	21.8	28:1

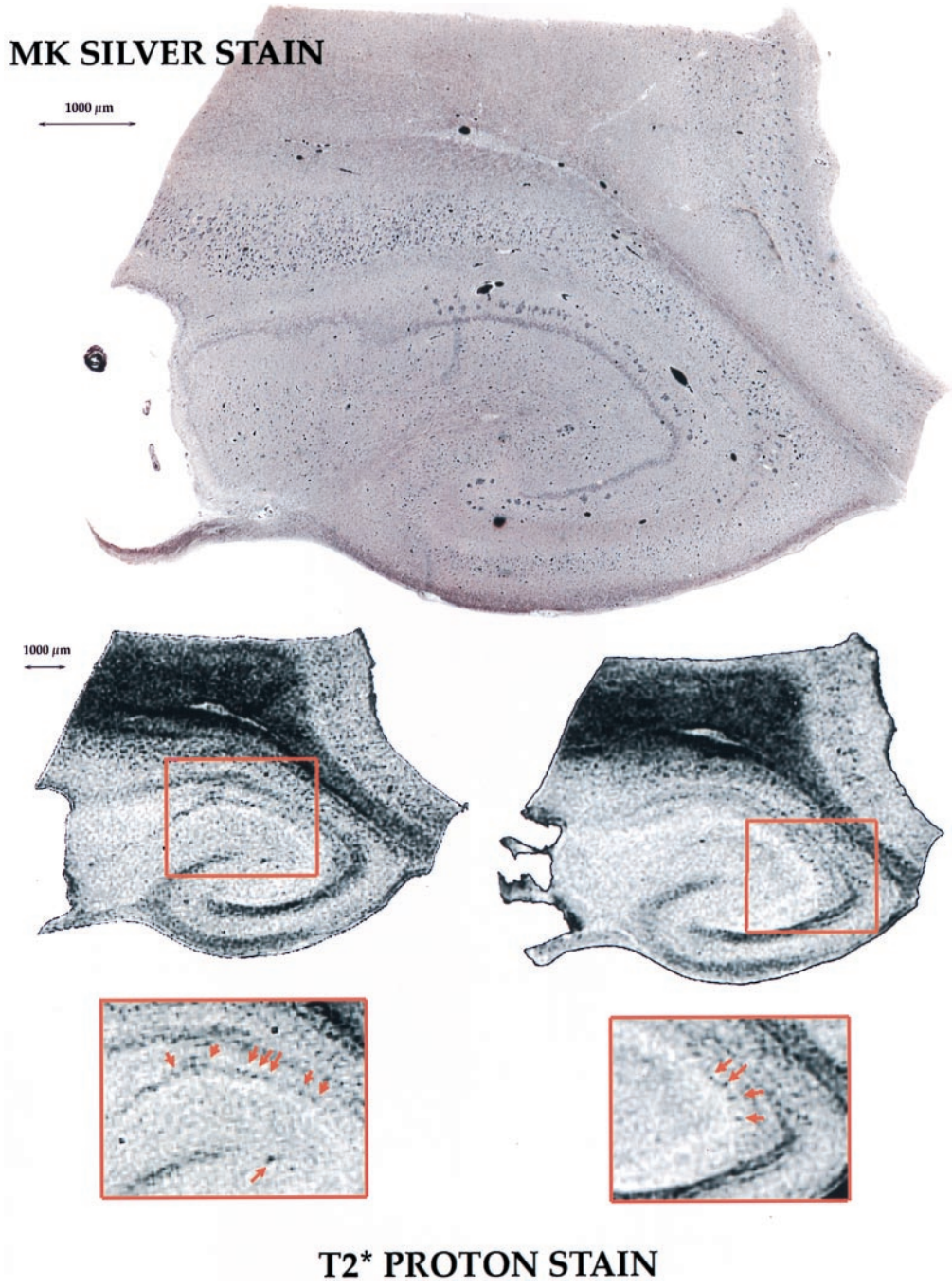

Fig. 4. Another example of plaque visualization on a T2* proton stain. A row of plaques can be seen on the MK silver-stained section in parallel to the granule cell layer. On the T2* proton stain, the granule cell layer can be identified as a faint, bright line. Above this bright layer, a row of black, rounded elements can be visualized. This particular hippocampal specimen was from a subject diagnosed with severe AD (Braak and Braak stage VI; ref. 11).

MRM. Thus, individual neuritic plaques in hippocampal tissue were visualized on T2*-weighted MRM images with optimized voxel sizes and SNR. Our results were derived from an extensive image analysis involving comparisons of MRM images with MK silver-stained sections. It proved extremely challenging to precisely match histological sections with MRMs. A successful match between the two-modality images was dependent on several factors. First, an optimized CNR and voxel size in the MRM images was essential to visualize a sufficient number of larger, permeating anatomical structures such as the alveus, fimbria, and hippocampal sulcus. Second, specific anatomical landmarks (e.g., uniquely shaped vessels) in association with the appearance of neuritic plaques on MK silver-stained sections were required to demonstrate convincingly (or not demonstrate) plaques on the proton stains. Many neuritic plaques probably went "unnoticed" on the high-resolution T2* proton stains because of lack of anatomical landmarks.

One of the most difficult aspects of this study was the inability to control the preparation of the samples. For example, the time period from death of the subject to tissue harvesting varied. Further, the hippocampal tissue specimens were formalin-immersion-fixed for variable periods of time before entering into our imaging experiment. Finally, the tissue samples varied in size

and this interfered with how efficiently the tissue was formalin-fixed at the time of harvesting. All these variables probably had an important effect on the quality and reproducibility of the scans from sample to sample and could explain the rather large SNR variations between images (e.g., in the T2* proton stains with voxel sizes of 5.9×10^{-5} mm^3, specimen 764 had an average SNR of 25:1, whereas in hippocampal specimen 511, SNR was 38:1). Another possible explanation for the large SNR variations could be that some tissue specimens were exposed to more motion during imaging, causing an overall reduction in the SNR. The strong magnetic field gradients could induce microscopic (microphonic) motions in the specimen if it was not sufficiently immobilized within the acrylic well during imaging.

The spatial resolution required for detection of individual plaque-like structures was 5.9×10^{-5} mm^3. In T2* proton stains acquired with larger voxel sizes, individual plaques were not visualized because of the partial volume artifact. This artifact arises because pixels have a finite volume and those that straddle a boundary between two structures effectively average the signal of the two regions and display an intermediate brightness. Thus, a voxel size of $\approx 40\ \mu m \times 40\ \mu m \times 40\ \mu m$ (5.9×10^{-5} mm^3) in the T2* images was necessary to visualize individual, 100-μm-wide plaques.

The mechanism by which neuritic plaques are detected by T2* could be explained if the plaque content of amyloid is diamagnetic and/or possesses paramagnetic properties [for example, if they contain metals (6)]. In both situations, spherical amyloid deposits might create complex local distortions in the magnetic field around the plaque (diamagnetic) and within the plaque itself (paramagnetic), causing its signal to decrease. This so-called "susceptibility" phenomenon would be enhanced by T2* contrast because spins are not refocused in the gradient-recalled echo [for review of this subject, see Callaghan (18)].

It was surprising that we were unable to demonstrate neuritic plaques on diffusion proton stains. We hypothesized that if amyloid might disturb normal fiber orientation when extracellularly deposited in white matter areas (e.g., molecular layer of the dentate gyrus), it should be detectable by diffusion contrast. For example, in experimental allergic encephalomyelitis, small, 100-μm-wide white matter lesions are readily visible by diffusion contrast (19). The most likely explanation for our failure to detect neuritic plaques by diffusion contrast is that the plaques had low proton density and/or very short T2. The short T2 is clearly evident in the T2* images because the plaques are dark. The diffusion proton stains invariably yielded lower SNR compared with T2* proton stains (using identical number of excitations and voxel sizes), and this could be caused by microscopic motion invoked by the gradients. Diffusion is inherently more sensitive to motion than other MR parameters (20).

Our results have shown that it is possible to detect neuritic plaques *in vitro* with T2* contrast at a voxel resolution of 5.9×10^{-5} mm^3 and a SNR of $\approx$30:1. Future and ongoing efforts are focused on applying this technology *in vivo*, for example, on different transgenic rodents overexpressing β-amyloid protein (21–23). Theoretically, what would it take to detect neuritic plaques *in vivo*? Currently at our Center, we routinely acquire *in vivo* mouse brain MR microscopy images at a spatial resolution of $\approx 50\ \mu m \times 50\ \mu m \times 500\ \mu m$ by using scan times of 2–3 hr. The SNR of these images are typically $\approx$20:1. Simply reducing the voxel size to $50\ \mu m \times 50\ \mu m \times 50\ \mu m$ would cause the images to suffer a 10-fold signal loss (SNR would be reduced to 2:1) and they would be too noisy to be meaningful for interpretation. Thus, for adequate tissue differentiation and plaque detection in high-resolution *in vivo* images, it would be necessary to recover sufficient SNR (at least SNR of 20:1). Merely prolonging scan time is not a viable option in fragile, anesthetized transgenic mice. For example, to recover a 10-fold signal loss, scan time also would have to be increased 10-fold, yielding a scan time of $\approx$200 hr!

A more practical solution to recover SNR would be to use a high-temperature superconducting (HTS) RF coil (24) instead of a conventional copper coil for imaging. The HTS coil previously has been shown to yield a 7-fold increase in SNR compared with conventional copper coil images (25). We estimate that a new generation of HTS coils under development will yield an $\approx$5-fold increase in SNR for *in vivo* studies. Further, MR contrast agents administered in optimal dosages might also increase SNR in high-resolution images by reducing T1. We currently are working on implementing these new technologies in our *in vivo* imaging studies of transgenic rodents overexpressing β-amyloid protein. Clearly, the ability to detect and follow the early progression of amyloid-positive brain lesions will greatly aid and simplify the many possibilities to intervene pharmacologically in AD. Ultimately, results gained from such studies would benefit humans afflicted with AD and related neurodegenerative disorders.

We thank Carlyn K. Rosenberg for processing and collecting much of the tissue at autopsy, John Ervin for histological cutting and staining, Sally L. Gewalt for help with the 3D visualization, and Elaine G. Fitzsimons for editorial assistance. This research project was supported by funds from the Alzheimer's Association, a Paul Beeson Physician Faculty Scholarship to H.B., and National Institutes of Health Research Grants NCRR P41 RR05959 and AG05128.

1. Johnson, G. A., Benveniste, H., Black, R. D., Hedlund, L. W., Maronpot, R. R. & Smith, B. R. (1993) *Magn. Reson. Q.* **9,** 1–30.
2. Johnson, G. A., Benveniste, H., Engelhardt, R. T., Qui, H. & Hedlund, L. W. (1997) *Ann. N. Y. Acad. Sci.* **820,** 139–148.
3. Smith, B., Linney, E., Huff, D. & Johnson, G. (1996) *Comp. Med. Imag. Graphics* **20,** 483–490.
4. Probst, A., Langui, D. & Ulrich, J. (1991) *Brain Pathol.* **1,** 229–239.
5. Esiri, M. M., Hyman, B. T., Beyreuther, K. & Masters, C. L. (1997) in *Greenfield's Neuropathology*, eds. Graham, D. I. & Lantos, P. L. (Arnold, London), Vol. 2, pp. 153–234.
6. Bouras, C., Giannakopoulos, P., Good, P. F., Hsu, A., Hof, P. R. & Perl, D. P. (1997) *Eur. Neurol.* **38,** 53–58.
7. Tokutake, S., Nagase, H., Morisaki, S. & Oyanagi, S. (1995) *Neurosci. Lett.* **185,** 99–102.
8. Huesgen, C., Burger, P. C., Crain, B. J. & Johnson, G. A. (1993) *Neurology* **43,** 145–152.
9. Hulette, C. M., Welsh-Bohmer, K. A., Crain, B., Szymanski, M. H., Sinclaire, N. O. & Roses, A. D. (1997) *Arch. Pathol. Lab. Med.* **121,** 615–618.
10. Mirra, S. S., Gearing, M., McKeel, D. W., Jr., Crain, B. J., Hughes, J. P., van Belle, G. & Heyman, A. (1994) *J. Neuropathol. Exp. Neurol.* **53,** 303–315.
11. Braak, H. & Braak, E. (1991) *Acta Neuropathol.* **82,** 239–259.
12. Banson, M. L., Cofer, G. P., Black, R. & Johnson, G. G. (1992) *Invest. Radiol.* **27,** 157–164.
13. Stejskal, E. O. (1965) *J. Chem. Phys.* **43,** 3597–3603.
14. Edelstein, W. A., Bottomley, P. A. & Pfeifer, L. M. (1984) *Med. Phys.* **11,** 180–185.
15. Lloyd, B., Brinn, N. & Burger, P. C. (1985) *J. Histotechnol.* **8,** 155–156.
16. Duvernoy, H. M. (1998) *The Human Hippocampus: Functional Anatomy, Vascularization and Serial Sections with MRI* (Springer, Berlin).
17. Crain, B. J. & Burger, P. C. (1988) *Acta Neuropathol.* **76,** 87–93.
18. Callaghan, P. T. (1993) *Principles of Nuclear Magnetic Resonance Microscopy* (Clarendon, Oxford).
19. Ahrens, E. T., Laidlaw, D. H., Readhead, C., Brosnan, C. F., Fraser, S. E. & Jacobs, R. E. (1998) *Magn. Reson. Med.* **40,** 119–132.
20. Moseley, M. E., Cohen, Y., Kucharczyk, J., Mintorovitch, J., Asgari, H. S., Wendland, M. R., Tsuruda, J. & Norman, D. (1990) *Radiology* **176,** 439–446.
21. Games, D., Adams, D., Alessandrini, R., Barbour, R., Berthelette, P., Blackwell, C., Carr, T., Clemens, J., Donaldson, T., Gillespie, F., *et al.* (1995) *Nature (London)* **373,** 523–527.
22. Hsiao, K. K., Borchelt, D. R., Olson, K., Johannsdottir, R., Kitt, C., Yunis, W., Xu, S., Eckman, C., Younkin, S., Price, D., *et al.* (1995) *Neuron* **15,** 1203–1218.
23. Hsiao, K., Chapman, P., Nilsen, S., Eckman, C., Harigaya, Y., Younkin, S., Yang, F. & Cole, G. (1996) *Science* **274,** 99–102.
24. Black, R. D., Early, T. A., Roemer, P. B., Mueller, O. M., Morgo-Campero, A., Turner, L. G. & Johnson, G. A. (1993) *Science* **259,** 793–795.
25. Hurlston, S. E., Brey, W. W., Suddarth, S. A., Yap, M. & Johnson, G. A. (1999) *Magn. Reson. Med.* **41,** 1032–1038.